

Wide-field prime-focus Imaging Atmospheric Cherenkov Telescopes: A systematic study

Albert Schliesser^{*}, Razmick Mirzoyan

Max-Planck-Institut für Physik, Föhringer Ring 6, D-80805 München, Germany

Abstract

By means of third-order optical theory as well as ray-tracing simulations we have investigated the feasibility of wide-field imaging atmospheric Cherenkov telescopes with a reflective prime-focus design. For a range of desired optical resolutions, we have determined the largest available field-of-view of single-piece spherical, single-piece parabolic, tessellated spherical, tessellated parabolic and Davies–Cotton designs, always considering a wide range of design parameters. The Davies–Cotton design exhibits a surprising similarity to the tessellated parabolic design in its qualitative behaviour. Also, elliptic telescope designs with better off-axis imaging properties than Davies–Cotton are presented. We show that by using $f/2$ optics it is possible to build prime-focus telescopes with a full field-of-view of 10° at 0.1° resolution.

Key words: Gamma-ray astronomy; Imaging atmospheric Cherenkov telescope; Wide-angle optics

PACS: 95.55.Ka, 95.75.Qr

References

- [1] T. C. Weekes, et al., Observation of TeV gamma rays from the Crab nebula using the atmospheric Cherenkov imaging technique, *Astrophysical Journal* 342 (1989) 379–395.
- [2] A. Kawachi, et al., The optical reflector system for the CANGAROO-II imaging atmospheric Cherenkov telescope, *Astropart. Phys.* 14 (2001) 261–269.

^{*} Corresponding author. Tel./Fax. +49-89-32354-328
Email address: `aschlies@mppmu.mpg.de` (Albert Schliesser).

- [3] K. Bernlöhr, et al., The optical system of the H.E.S.S. imaging atmospheric Cherenkov telescopes. Part I: layout and components of the system, *Astropart. Phys.* 20 (2003) 111–128.
- [4] J. Fernandez, R. Mirzoyan, V. Fonseca, J. C. Gonzales, E. Lorenz, Optics of the MAGIC telescope, Appendix A of J. A. Barrio et al., *The MAGIC Telescope*, MPI-PhE/98-5, Max-Planck-Institut für Physik (1998).
- [5] T. C. Weekes, et al., VERITAS: the Very Energetic Radiation Imaging Telescope Array System, *Astropart. Phys.* 17 (2002) 221–243.
- [6] T. Kifune, Y. Takahashi, World wide network for future observations: All sky monitor at VHE energies, in: O. C. de Jager (Ed.), *Proc. "Towards a Major Atmospheric Cerenkov Detector V"*, Kruger National Park, South Africa, 1997, pp. 315–322.
- [7] D. Korsch, *Reflective Optics*, Academic Press, 1991.
- [8] Zemax Development Corporation, ZEMAX EE.
- [9] J. M. Davies, E. S. Cotton, Design of the quartermaster solar furnace, *J. Solar Energy Sci. Eng.* 1 (1957) 16–21.
- [10] D. A. Lewis, Optical characteristics of the Whipple observatory TeV gamma ray imaging telescope, *Exp. Astron.* 1 (1990) 213–226.
- [11] N. Tonello, *Misure ottiche et strategie di trigger per il telescopio MAGIC*, diploma thesis, University of Padua (2002).
- [12] A. Akhperjanian, V. Sahakian, Performance of a 20 m diameter Cherenkov imaging telescope, *Astropart. Phys.* 21 (2004) 149–161.
- [13] R. Mirzoyan, V. Fomin, A. Stepanian, On the optical design of VHE gamma ray imaging Cherenkov telescopes, *Nucl. Instrum. Methods A* 373 (1996) 153–158.

1 Introduction

The first strong γ -ray signal in the TeV energy range has been measured by the Whipple collaboration from the Crab Nebula in 1989 [1]. Since then the technique of ground-based imaging atmospheric Cherenkov telescopes (IACTs) has substantially improved. Nowadays the ground-based IACT technique is the most sensitive method for measuring very high energy (VHE) γ -rays from celestial objects. The CANGAROO [2], HESS [3], MAGIC [4] and VERITAS [5] telescopes are currently the largest and the most sensitive instruments measuring the sky in γ -rays from four continents. Although differing in detail, their optics are all prime-focus systems consisting of a single, large-aperture, segmented reflector and a 2-dimensional detector array in the focal plane. These systems are delivering highly interesting scientific data, although some

of them are not yet in their final configuration. In the next 2-3 years they will be completed and put into operation at their full power. The community hopes that these improved instruments will increase the number of established VHE γ -ray sources by one order of magnitude.

The evaluation of the scientific outcome might eventually also reveal which demands the next-generation instrumentation should meet. In recent years one of the frequently discussed designs are wide-angle IACTs [6]. By using wide-angle, highly sensitive, large telescopes of very low threshold energy setting one can perform all-sky surveys in a short time. In order to discriminate images induced by γ -ray showers from those of much more abundant hadrons an optical resolution of $\sim 0.1^\circ$ is required over the entire field-of-view (FOV). Below 100 GeV, even ≥ 2 times better resolution is needed, since the differences in the images of γ -ray- and hadron-induced showers become smaller at lower energies. Thus, depending on the desired resolution, the FOV of present-day IACTs is limited to below 5° .

In the following, we present an exhaustive analysis of the common IACT designs with respect to their wide-field performance. For that purpose, we have analysed optical spot sizes as a function of focal ratio, incidence angle and mirror segment size by means of both analytical third-order geometrical optics and ray-tracing simulations.

2 Methods

Both approaches used in this paper are capable of determining the optical spot size: By using third-order optical theory, on the one hand, one can readily assess a given system by evaluating analytically derived formulae. Yet, its results are only approximative and the theory can hardly be applied to tessellated geometries. Ray-tracing simulations, on the other hand, can predict optical performance very accurately, but require proper simulation of every given system and parameter set.

2.1 Parameters and properties of prime focus systems

The basic geometry of a simple prime focus system is depicted in *Fig. 1*. Every ray is incident on the reflector in a point $(x, y, z(x, y))$, is reflected and hits the image plane in (ξ, η, f) , where f is the focal length of the system. Here, $z(x, y)$ is the reflector surface function. The reflector and image coordinate systems are supposed to be aligned such that $\vec{e}_\xi \parallel \vec{e}_x$ and $\vec{e}_\eta \parallel \vec{e}_y$, but are offset along the global z -axis by the focal distance f . Although in general,

the image surface could be curved and offset along the z -axis to correct for aberrations, we will only consider the simpler case of a fixed and flat image surface. For IACTs, these are realistic assumptions.

The angular object coordinates (ϕ_x, ϕ_y) determine the angles the incident rays make with the z -axis. Single-piece reflectors have full rotational symmetry which is only slightly disturbed by segmentation to the analyzed extent. For this reason, an analysis with $\phi_y = 0$ imposes no restriction, and we may simply distinguish the *tangential* image coordinate (parallel to the projection of the incident ray into the image plane) and the *sagittal* image coordinate (perpendicular to the projection of the incident ray into the image plane): If $\phi_x \neq 0 = \phi_y$, then ξ is the tangential, and η the sagittal image coordinate.

For a given incidence angle ϕ_x , rays incident on different reflector loci hit the image (camera) plane at slightly different points due to aberrations. The mean values $(\langle \xi \rangle, \langle \eta \rangle)$ of all incoming rays' image coordinates define the image *centroid*. The *rms point spread*, the root-mean-square deviations

$$\begin{aligned}\Delta\xi &= \sqrt{\langle (\xi - \langle \xi \rangle)^2 \rangle} && \text{(tangential rms)} \\ \Delta\eta &= \sqrt{\langle (\eta - \langle \eta \rangle)^2 \rangle} && \text{(sagittal rms)}\end{aligned}\tag{1}$$

of the rays' actual image coordinates from the centroid position, are a reasonable measure of the optical spot size.

Imaging mirrors commonly are surfaces of revolution defined by conic sections. They are characterized by three parameters, namely their radius of curvature r , their diameter d and their conic constant δ . Their surface equation reads

$$z(x, y) \equiv z(h) = \frac{1}{r} \cdot \frac{h^2}{1 + \sqrt{1 - (1 + \delta)h^2/r^2}}\tag{2}$$

with $h := \sqrt{x^2 + y^2} \leq d/2$. Parabolic and spherical shapes are obtained by setting $\delta = -1$ and $\delta = 0$, respectively.

In the simplest case, the reflector of a telescope consists of one single large mirror with its surface defined by (2). Though, due to the large apertures and cost reasons, the reflectors of existing IACTs are segmented into considerably smaller mirrors, which are mounted on a common reflector dish. The individual mirror segments are conic sections of revolution. For ease of fabrication and testing, they are mostly chosen to be spherical.

We assume the individual mirrors of such a tessellated reflector are square-shaped, and mounted on a square grid in (x, y) such that the four inmost mirrors touch $(0, 0)$ with one edge. The z -coordinate of the mirror centers is

defined by the *gross reflector shape*, which itself is a conic section of revolution. The size of the segments is expressed in terms of the *tessellation ratio*

$$\alpha = \frac{\text{size of individual mirror}}{\text{diameter of reflector}}. \quad (3)$$

Tessellation may introduce further aberrations, since the actual shape of the reflector deviates from the (putatively) ideal shape of a single reflector. Alignment accuracy may also influence the optical quality strongly. Interestingly, tessellation also introduces new degrees of freedom to the optical design: An individual mirror's orientation (i. e. the normal to its surface) can be chosen independently of the normal to the gross shape at this mirror's location.

2.2 Third-order analysis

Third-order optical theory has been developed for optical engineering tasks before the advent of fast computers. It is capable of readily anticipating optical performance of a given system and its dependence on design parameters once an appropriate formula has been derived from its basic rules. Although in principle it could also be applied to tessellated systems, its elegant simplicity would be lost due to the need of summation over a large number of single mirrors. For that reason, its application will be limited to single mirror systems in this study. Only in the limit of small tessellation ratios, third-order results apply to tessellated systems as well.

When a ray with angular object coordinates (ϕ_x, ϕ_y) hits a single-piece reflector in $(x, y, z(x, y))$, then from third-order aberration theory [7], an approximate expression for the image coordinates can be derived to be

$$\begin{aligned} \xi &= -\frac{h^2(x(1+\delta) + 2f\phi_x) + 4f(2f^2\phi_x + (x + 2f\phi_x)(x\phi_x + y\phi_y))}{8f^2} \\ \eta &= -\frac{h^2(y(1+\delta) + 2f\phi_y) + 4f(2f^2\phi_y + (y + 2f\phi_y)(x\phi_x + y\phi_y))}{8f^2}. \end{aligned} \quad (4)$$

By integrating x and y over a circular aperture with $h \leq d/2$, analytic expressions for the rms point spread (1) can immediately be given as

$$\begin{aligned} \Delta\xi_{\text{fps}} &= \frac{1}{4} \sqrt{\frac{(1+\delta)^2}{2048} \left(\frac{d}{f}\right)^6 + \frac{(6+4\delta)\phi_x^2 + \phi^2}{96} \left(\frac{d}{f}\right)^4 + \phi_x^2\phi^2 \left(\frac{d}{f}\right)^2} \\ \Delta\eta_{\text{fps}} &= \frac{1}{4} \sqrt{\frac{(1+\delta)^2}{2048} \left(\frac{d}{f}\right)^6 + \frac{(6+4\delta)\phi_y^2 + \phi^2}{96} \left(\frac{d}{f}\right)^4 + \phi_y^2\phi^2 \left(\frac{d}{f}\right)^2}, \end{aligned} \quad (5)$$

using the abbreviation $\phi := \sqrt{\phi_x^2 + \phi_y^2}$. These expressions still simplify considerably if we set $\phi_y = 0$ as discussed before, this substitution was deferred in order to show the symmetry of the system. The index “fps” indicates that the results are expressed in the focal plane scale, i. e. they have been divided by the focal length of the system to yield an angular quantity. It will be omitted for the sake of shortness in some places; generally, if the rms point spread is given in angular units, the focal plane scaling applies. The expressions (5) immediately give performance estimates for all conceivable single-piece reflectors by simply plugging in the corresponding parameters characterizing the system.

2.3 Ray tracing

Complementary to the analytic, yet approximative third-order analysis, ray tracing simulations yield precise performance data for imaging systems, including also the more complex tessellated reflector geometries.

Both, a commercially available optical simulation package [8] and a self-implemented ray-tracer were used. With its intuitive graphical user interface and its powerful analysis tools, the commercial package allows one comfortable editing and detailed evaluation of the systems under consideration. Though, simulations of tessellated reflectors with their large number of single optical elements¹ are cumbersome to implement and require very long simulation run times. For that reason, a custom ray-tracing engine was programmed. The parallelized C-code can be run as a stand-alone simulation or used from within the commercial program to enable the combination of tessellated reflectors with other optical elements. Arbitrary tessellated reflector geometries are supported and easy to set up.

3 Results

Comprehensive simulations have been made for the cases of (1.1) single-piece spherical, (1.2) single-piece parabolic, (2.1) tessellated spherical, (2.2) tessellated parabolic design with constant radii of curvature, (2.3) Davies–Cotton and (2.4) tessellated parabolic design with adjusted radii of curvature. For every design, systems with focal lengths f ranging from 1.0 to 2.9 in steps of 0.1 were investigated. Since the diameter of the reflector was set to 1 in all systems, *focal ratios* f/d equally range from 1.0 to 2.9. For tessellated systems, the tessellation ratio was varied from 0.005 to 0.080 in steps of 0.005. Image

¹ Simulations with up to > 100000 single mirrors have been made.

quality was analyzed for incidence angles between 0.0° and 5.8° in steps of 0.2° by means of tracing ~ 800000 rays through the system and determining the rms point spread (1) of the resulting images. The simulation results are presented in the following section together with some implications from third-order theory.

3.1 Single-piece reflectors

3.1.1 Single-piece sphere

Inserting $\delta = 0$ for a spherical reflector into (5) and setting $\phi_y = 0$ one obtains

$$\begin{aligned}\Delta\xi_{\text{fps}} &= \frac{1}{4}\sqrt{\frac{1}{2048}\left(\frac{d}{f}\right)^6 + \frac{7\phi_x^2}{96}\left(\frac{d}{f}\right)^4 + \phi_x^4\left(\frac{d}{f}\right)^2} \\ \Delta\eta_{\text{fps}} &= \frac{1}{4}\sqrt{\frac{1}{2048}\left(\frac{d}{f}\right)^6 + \frac{\phi_x^2}{96}\left(\frac{d}{f}\right)^4}\end{aligned}\tag{6}$$

for the rms point spread in tangential and sagittal direction, respectively. *Spherical aberration*, corresponding to the first summand in (6), strongly deteriorates imaging quality especially for small incidence angles. In order to get $\Delta\xi_{\text{fps}}$ and $\Delta\eta_{\text{fps}}$ below 0.05° , the focal ratio must be larger than 1.85, as can be derived from (6). This is confirmed by the simulation results, which are shown in Fig. 2. The sagittal rms hardly changes with the light incidence angle as it is dominated by spherical aberration in the depicted parameter range. In contrast, the tangential rms displays also a considerable angular dependence. The overall behaviour of the system is predicted by third-order theory with quantitative deviations smaller than 10%.

3.1.2 Single-piece paraboloid

Let us now insert the value $\delta = -1$ for a single-piece parabolic reflector into (5) and consider again the case $\phi_y = 0$:

$$\begin{aligned}\Delta\xi_{\text{fps}} &= \frac{1}{4}\sqrt{\frac{3\phi_x^2}{96}\left(\frac{d}{f}\right)^4 + \phi_x^4\left(\frac{d}{f}\right)^2} \\ \Delta\eta_{\text{fps}} &= \frac{1}{4}\sqrt{\frac{\phi_x^2}{96}\left(\frac{d}{f}\right)^4}\end{aligned}\tag{7}$$

From the obtained formulae (7) one can notice that the first summands in the square roots of (5) have vanished so that on-axis imaging is supposed

to be perfect for arbitrary focal ratios. Though, at non-zero incidence angles, the aberrations described by the second (*coma*) and third (*astigmatism*) summands induce a blurring of the image, which increases progressively with the incidence angle. The simulation results, illustrated in *Fig. 3*, confirm the predictions.

3.2 Tessellated reflectors

3.2.1 Tessellated spherical design

A single spherical reflector can be segmented into smaller mirrors. If the small mirrors are spherical themselves and have the same radius of curvature as the gross sphere their surfaces coincide with the gross shape. Apart from possible small gaps between the individual mirrors, the tessellated reflector surface is then identical to the single-piece spherical reflector's. Correspondingly, the simulation yields also the same performance data, as illustrated in *Fig. 4*.

3.2.2 Tessellated parabolic design with constant radii of curvature

The simplest way to segment a parabolic reflector into smaller mirrors is the following: The individual mirrors are spherical, have all the same radius of curvature, namely twice the focal length f of the telescope, and their normals (in the center) coincide with the normal of the gross reflector shape at their center. *Fig. 5* shows the simulation results for such a configuration for a realistic tessellation ratio $\alpha = 0.03$. Qualitatively, they are very similar to the results for the single piece paraboloid. Only when approaching $\phi_x = 0$, where imaging of a single-piece parabola of revolution becomes perfect, the influence of tessellation reduces image quality.

3.2.3 Davies–Cotton design

Another tessellated reflector design being applied in some of today's IACTs originally goes back to a solar concentrator and is termed Davies–Cotton design [9]. In this design, the spherical mirror elements are arranged on a spheroid with the radius being just the focal length of the telescope. The radius of curvature of the individual mirrors is constantly $2f$. The normals of the mirrors do not coincide with the normals of the gross spheroid (radius f), instead they all point to $(x, y, z) = (0, 0, 2f)$. For on-axis incidence, the chief rays of the single mirrors are imaged perfectly into the focal point like in the case of a tessellated parabolic reflector [10]. The results for the Davies–Cotton design (*Fig. 6*) exhibit a striking similarity to the data for a parabolic reflector, although its gross shape is spherical. For larger incidence angles, this design

outperforms the parabolic configuration.

3.2.4 Tessellated parabolic design with adjusted radii of curvature

The last presented design uses a parabolic gross shape which defines the positions and the orientation of the mirrors. Though, in contrast to the second discussed scenario, the radii of curvature of the mirrors are adapted to their varying distance to the focal point $(x, y, z) = (0, 0, f)$ in order to avoid defocus aberration of the individual mirror images.

A parabola of revolution has two principal radii in every point of its surface. As a first approximation, one may take the average of these two as the radius of curvature of a mirror segment. Yet, it turns out that especially for larger distances from the telescope axis, this is not an ideal solution. Superior choices of the radii have been found in numerical optimization runs [4], [11]. Interpolating and scaling the optimized radii for a parabolic gross shape from ref. [4], we obtain improved performance for small incidence angles, as the simulation data show (*Fig. 7*). Yet, for larger angles global comatic aberrations dominate – just as in the case of the tessellated parabolic reflector without radius adjustment of the single mirrors.

4 Discussion

4.1 Shower discrimination capability

The crucial criterion for an optical layout suitable for IACTs is the ability to discriminate showers induced by hadrons from those induced by γ -rays. In order to enable shower discrimination over a given FOV, a large enough focal ratio has to be chosen such that both tangential and sagittal rms spot sizes are below 0.05° .

Fig. 8 shows the minimum required focal ratios for the four presented tessellated reflector designs. The results have been obtained from the simulation data for the tangential rms, which is larger than the sagittal rms in all considered cases. Although third-order optical theory only treats single-piece reflectors, the behavior of the systems can be well predicted. Solving (5) for the focal ratio, good approximations for the results found in the simulations can be obtained. Only the Davies–Cotton data cannot be reproduced that accurate – this is because it is the only discussed design in which the normals (in the centers) of the individual mirrors do not coincide with the normals of the gross shape; a situation that cannot be captured by conventional third-order

analysis. Yet, qualitatively, the behavior resembles much that of a parabolic reflector.

The Davies–Cotton design is superior to all other presented designs: It allows to make reflectors ~ 0.2 faster for all analyzed fields compared to parabolic gross shapes. Adjusting the radius of curvature of the individual mirrors in a parabolic design is only effective when small FOV ($\phi < 1.5^\circ$) are desired. Spherical configurations yield the largest spot sizes and, consequently, only poor shower discrimination capability.

4.2 *Alternative configurations*

The Davies–Cotton design has no single-piece analogue but makes explicit use of the new degree of freedom introduced by tessellation. It is an interesting question whether there are other tessellated prime-focus systems with even wider FOV.

A simple approach was taken to answer this question. For fixed f and d , the parameters r and δ of the gross reflector shape were varied. Reasonable imaging of the whole system was warranted by orientating the individual mirrors (all of which have a radius of curvature of $2f$) so that their normals (at their centers) point to $(0, 0, 2f)$, like in a Davies–Cotton design [10]. Quite easily, designs allowing even wider FOV than conventional Davies–Cotton could be found, with some dependence on the chosen focal ratio. For $f/d = 2$, *Fig. 9* shows the example of an elliptical gross shape ($r = 0.85f$, $\delta = 5$) which has a full FOV of 10° .

Besides spatial resolution, high temporal resolution is important for an effective background suppression especially when measuring in the sub-100 GeV energy regime [12]. This means that the arrival time of Cherenkov photons at the camera should not depend on the point where they hit the reflector. Parabolic reflectors are (apart from small effects introduced by tessellation) *isochronous*, whereas in a Davies–Cotton design there is a spread in photon arrival time [13]. We have simulated the photon arrival time distribution for parabolic, Davies–Cotton and the described elliptic design in the limit $\alpha \rightarrow 0$ and summarize the main results in *Table 1*. The improved off-axis imaging of the elliptic design comes at the expense of timing accuracy. The differences in the photon arrival time distributions for different incidence angles $< 5^\circ$ were negligible in all considered designs.

4.3 Tessellation ratio

The data presented so far were for the fixed tessellation ratio of $\alpha = 0.03$, which corresponds approximately to the value of the MAGIC telescope, which has a diameter² of 17 m and the individual mirrors are $0.5 \text{ m} \times 0.5 \text{ m}$. Other ratios are imaginable and may also be desirable for cost reasons. As stated above, all simulations were performed for a range of tessellation ratios. Depending on the system configuration, the focal ratio and incidence angle, it may have influence on image quality within the investigated range. The data for a focal ratio of 1, and incidence angles 0° , 1° and 2° are shown in *Fig. 10*. The choice of these parameters has practical reasons: Focal ratios as fast as 1 or slightly more are common in today's IACTs, and the incidence angles are limited to below 3° .

The parabolic design shows the strongest dependence on the tessellation ratio. This is due to the defocus of the individual mirrors that worsens for larger segments. If defocus is eliminated by adjusting the radius of curvature in the parabolic design, the tessellation ratio is much less critical. Only for small incidence angles, when global aberrations vanish, it affects quality distinctly. As expected, the values of the parabolic configurations converge in the limit $\alpha \rightarrow 0$. For the spherical design, the tessellation ratio does not influence image quality, since the resulting shape is always the same – that of a solid spheroid – independent of segmentation. The aberrations are too large to fit in the range depicted in *Fig. 10*, though.

Obviously, tessellation ratio does not deteriorate imaging quality critically as long as it is below 0.08 (and the individual radii of curvature are adjusted in the parabolic case). Thus, for example, the mirrors of the MAGIC telescope could have twice the size (then $\alpha \approx 0.06$) without worsening its performance.

5 Conclusions

The main purpose of this paper was to study the potential of different prime focus designs for wide-angle IACTs, using third-order optical aberration theory and ray-tracing simulations. The investigations comprise practically the entire reasonable parameter range for both single-piece and tessellated parabolic and spherical, as well as the Davies–Cotton design. Along with that, some new tessellated designs have been examined. The Davies–Cotton design exhibits best off-axis performance of the conventional designs. Yet, tessellated designs with elliptic gross shapes can yield even wider FOV but at the expense of

² Actually, the MAGIC reflector is an octagon.

timing accuracy. We show that $f/2$ designs can provide 10° full FOV. For faster $f/1$ optics the full FOV available at a 0.1° resolution is below 3° . The simulation results also show that for wide-angle IACTs, segmentation of the gross shape into spherical mirrors deteriorates imaging only negligibly.

We are planning to study more complex systems that may provide even wider fields-of-view.

Acknowledgements

We gratefully acknowledge support from M. Teshima.

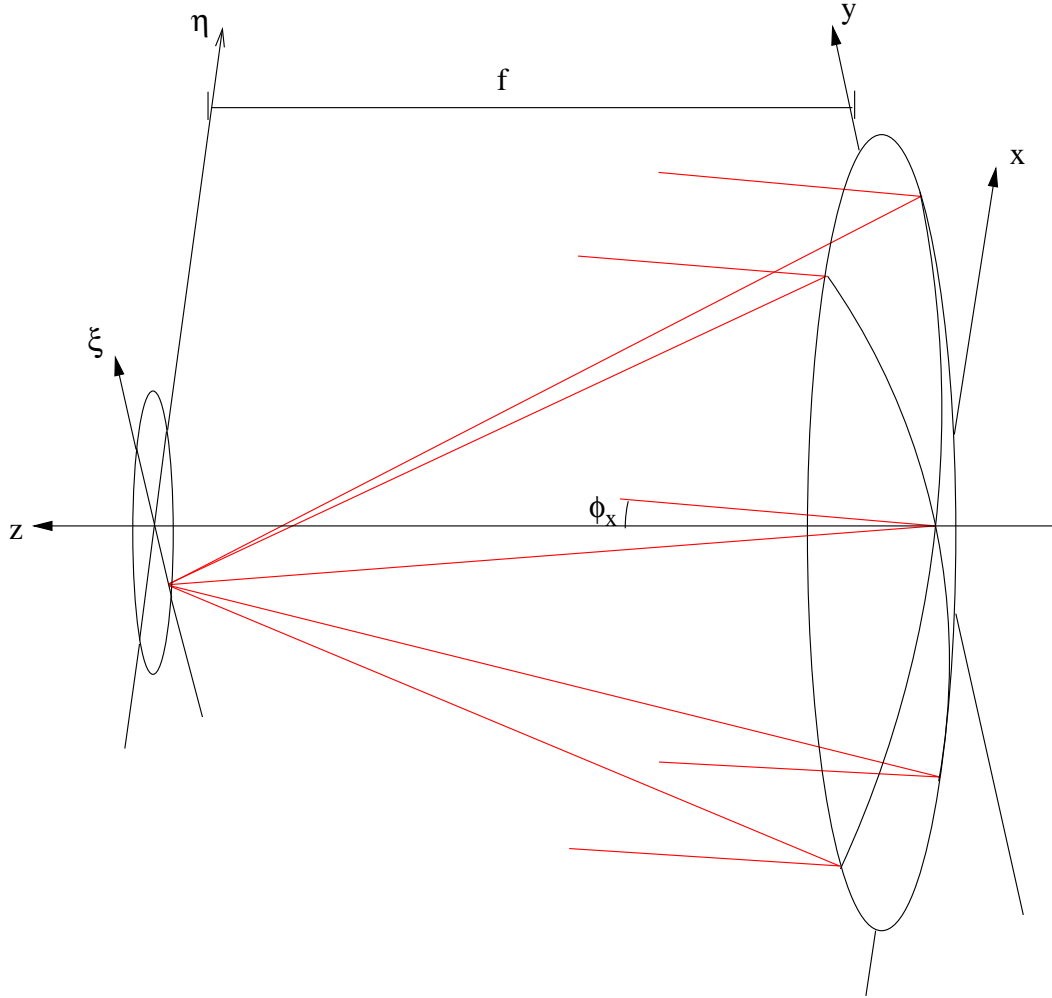


Fig. 1. Optical layout of a prime focus system. Coming from the left, the rays hit the mirror in coordinates $(x, y, z(x, y))$, are reflected and intercept the focal plane in (ξ, η, f) . Some examples of off-axis rays (red) with an incidence angle ϕ_x are indicated.

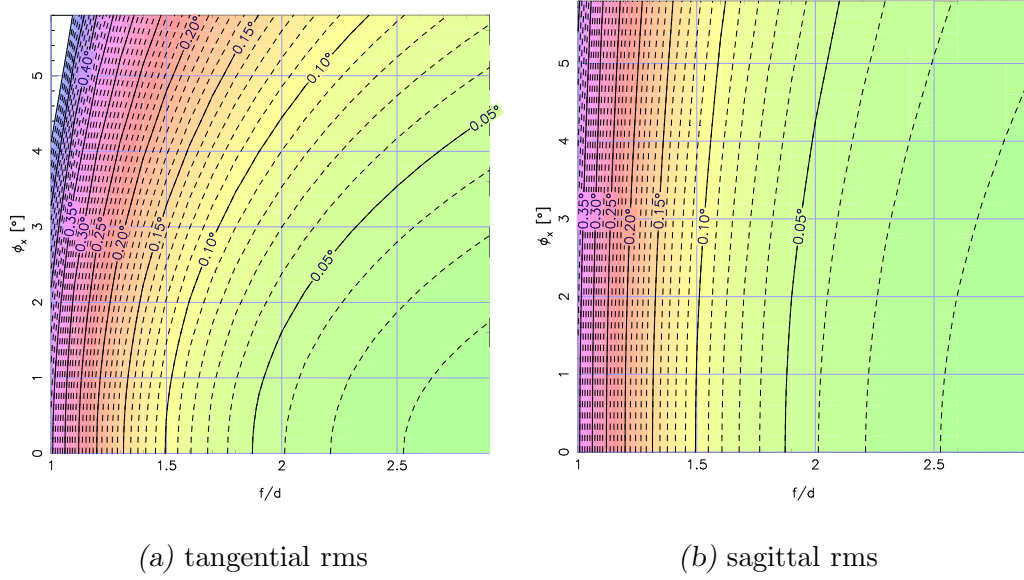


Fig. 2. Dependence of rms point spread on the incidence angle ϕ_x and the focal ratio f/d for a single-piece spherical reflector. The contour lines connect $(f/d, \phi_x)$ -combination which result in an equal rms spread. The line at 0.05° marks the upper limit for achieving γ -hadron discrimination.

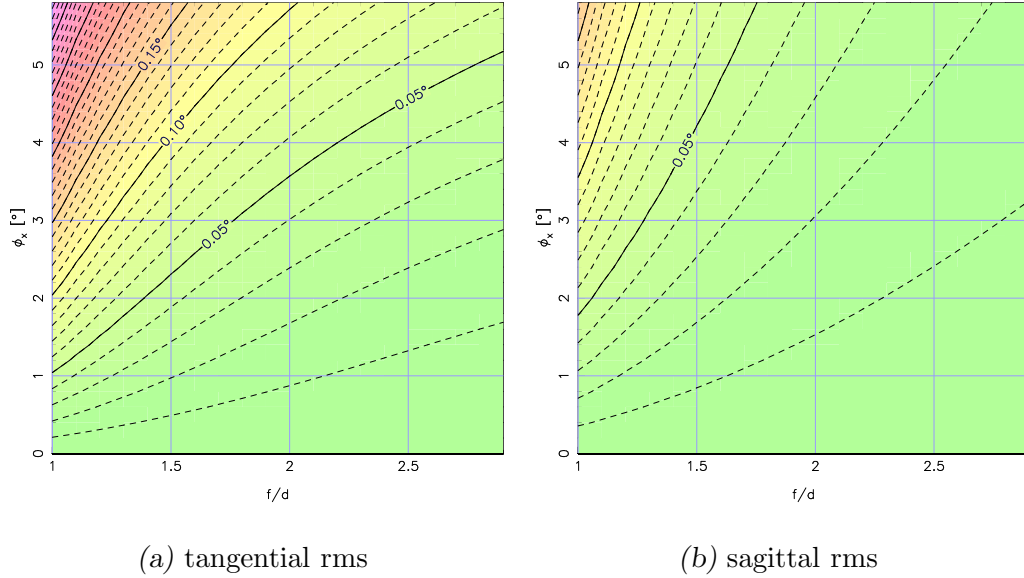
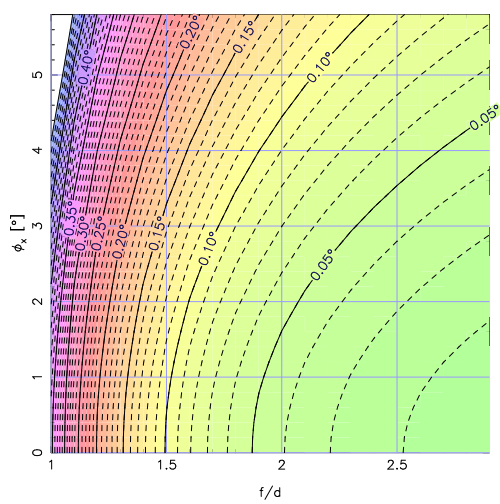
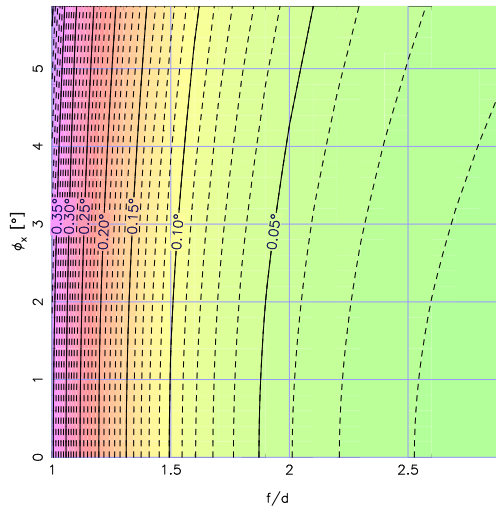


Fig. 3. Rms point spread for a single-piece parabolic reflector. Illustration analogous to Fig. 2.

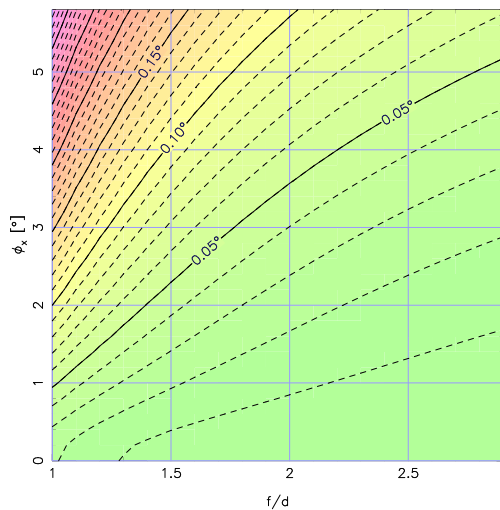


(a) tangential rms

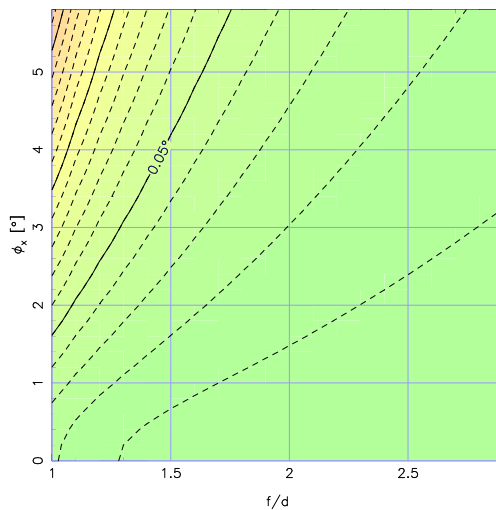


(b) sagittal rms

Fig. 4. Rms point spread for a tessellated spherical reflector. The tessellation ratio α is 0.03. Illustration analogous to Fig. 2.

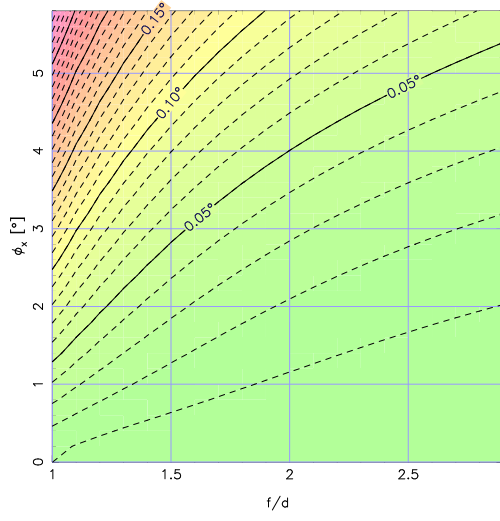


(a) tangential rms

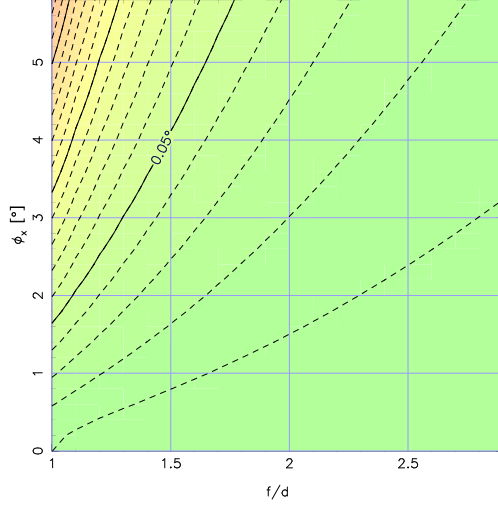


(b) sagittal rms

Fig. 5. Rms point spread for a tessellated parabolic reflector with constant radii of curvature. The tessellation ratio α is 0.03. Illustration analogous to Fig. 2.

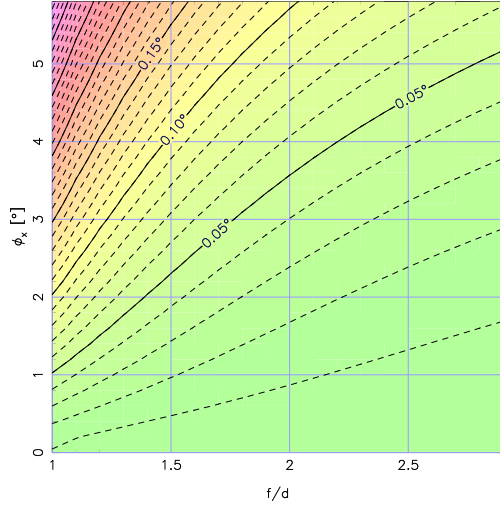


(a) tangential rms

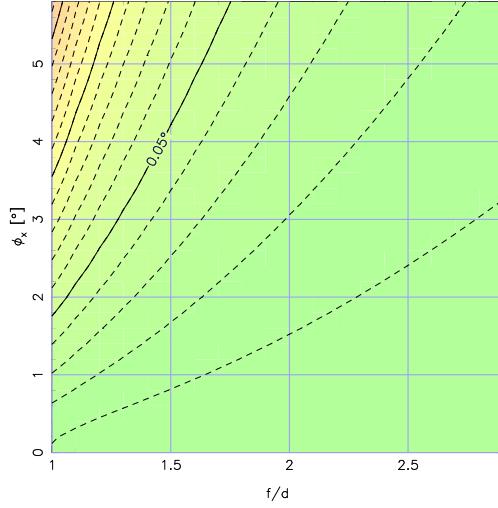


(b) sagittal rms

Fig. 6. Rms point spread for a Davies–Cotton reflector. The tessellation ratio α is 0.03. Illustration analogous to *Fig. 2*.



(a) tangential rms



(b) sagittal rms

Fig. 7. Rms point spread for a tessellated parabolic reflector with adjusted radii. The tessellation ratio α is 0.03. Illustration analogous to *Fig. 2*.

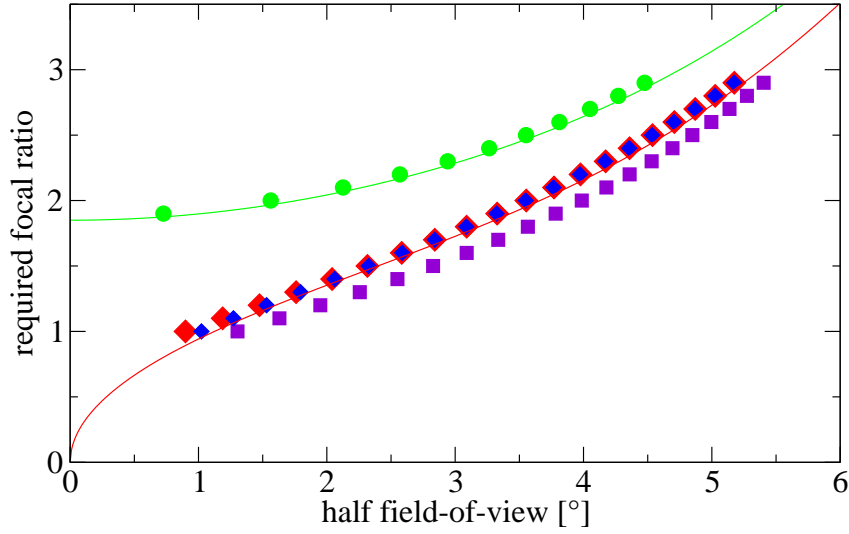


Fig. 8. Required focal ratio to distinguish γ -ray from hadron induced showers over a half FOV ϕ . Points: simulation data for spherical design (green), parabolic design with constant radii (red), Davies–Cotton design (violet), parabolic design with adjusted radii (blue). Tessellation ratio α is 0.03. Lines: third-order approximation for single-piece paraboloid (red), single-piece sphere (green).

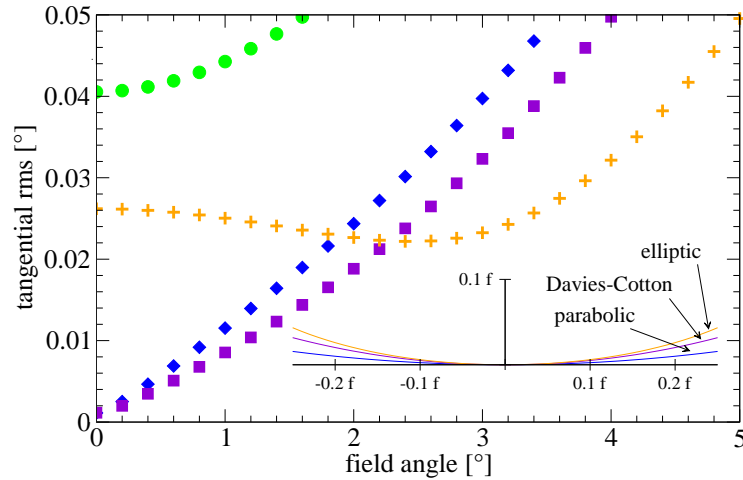


Fig. 9. Simulated tangential rms for given field angle ϕ for spherical design (green), Davies–Cotton design (violet), parabolic design with adjusted radii (blue), elliptical design (orange). The focal ratio is 2, tessellation ratio 0.03. The inset shows the actual gross shape of the different configurations.

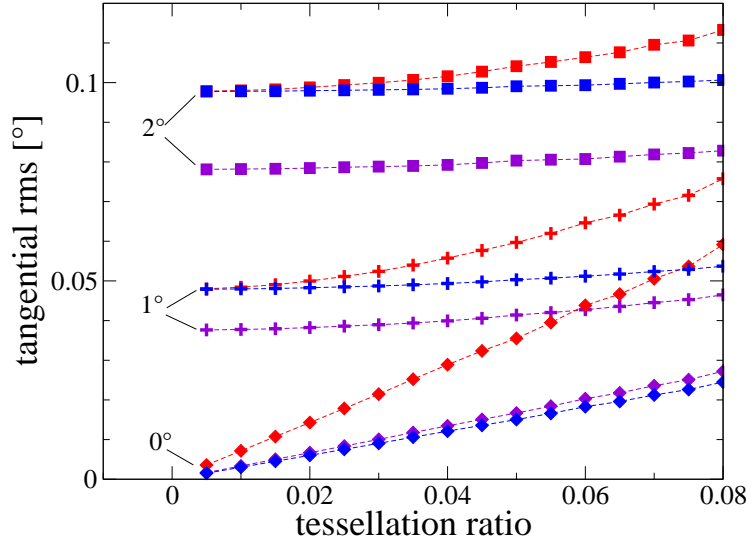


Fig. 10. Dependence of tangential rms on tessellation ratio α for incidence angles 0° (diamonds), 1° (crosses) and 2° (squares). Parabolic design with constant radii (red), Davies-Cotton design (violet), parabolic design (blue) with adjusted radii. Points are connected to guide the eye.

	r	δ	ϕ_{\max}	t_{FWHM}/f $\phi_x = 0^\circ$	t_{FWHM}/f $\phi_x = \phi_{\max}$
parabolic	$2f$	-1.0	$\sim 3.6^\circ$	0.00 ns/ m	0.00 ns/ m
Davies-Cotton	f	0.0	$\sim 4.0^\circ$	0.11 ns/ m	0.11 ns/ m
elliptic	$0.85f$	$+5.0$	$\sim 5.0^\circ$	0.18 ns/ m	0.18 ns/ m

Table 1

Comparison of point spread and timing properties of some tessellated designs with a gross shape described by the radius of curvature r and conic constant δ . The focal ratio is $f/d = 2$, the tessellation ratio $\alpha = 0.03$ for all systems. ϕ_{\max} is the maximum available half field angle and t_{FWHM} the full width at half maximum of the photon-arrival time distribution, neglecting tessellation ($\alpha \rightarrow 0$). Since t_{FWHM} scales linearly with the dimensions of the system for fixed f/d , it is given normalized to the focal distance.